Materials Today Bio 31 (2025) 101542

Contents lists available at ScienceDirect

Materials Today Bio

journal homepage: www.journals.elsevier.com/materials-today-bio

Mitochondria-targeted photothermal-chemodynamic therapy enhances checkpoint blockade immunotherapy on colon cancer

Benchao Zheng [a,b], Hongbo Wang [a,b], Shiyi Zhai [a,b], Jiangsheng Li [c], Kuangda Lu [a,b,*]

[a] Institute of Medical Technology, Peking University Health Science Center, Beijing, 100191, PR China
[b] Institute of Advanced Clinical Medicine, Peking University, Beijing, 100191, PR China
[c] Key Laboratory of Carcinogenesis and Translational Research of Ministry of Education, Key Laboratory for Research and Evaluation of Radiopharmaceuticals of National Medical Products Administration, Department of Nuclear Medicine, Peking University Cancer Hospital, Beijing, 100142, PR China

ARTICLE INFO

Keywords:
Mitochondria-targeting
Photothermal therapy
Chemodynamic therapy
Checkpoint blockade immunotherapy
Cancer

ABSTRACT

Immunotherapy has emerged as a hotspot for cancer treatment. However, the response rate of monotherapy remains relatively low in clinical settings. Photothermal therapy (PTT), which employs light energy to ablate tumors, can also activate tumor-specific immune responses. This effect has been attributed in several studies to the release of damage-associated molecular patterns (DAMPs) triggered by mitochondrial injury. We propose that mitochondria-targeted PTT may better synergize with immunotherapy. Herein, we constructed a multifunctional nanoplatform that enables mitochondria-targeted photothermal-chemodynamic combination therapy by conjugating indocyanine green-thiol (ICG-SH) and mercaptoethyl-triphenylphosphonium (TPP-SH) onto polyvinyl pyrrolidone (PVP)-coated gold-copper nanoparticles (AIT). Upon near-infrared light (NIR) irradiation, AIT ablates cancer cells and amplifies the effect of chemodynamic therapy (CDT), thereby inducing apoptosis in the tumor. The combination of CDT and PTT promotes immunogenic cell death, which could synergize with checkpoint blockade immunotherapy. In a bilateral mouse colon cancer model, we observed complete eradication of light-irradiated primary tumors and significant inhibition of distant untreated tumors in the group treated with AIT plus anti-PD-1 (αPD-1). We found a significant increase in serum levels of pro-inflammatory factors, including interleukin-6 (IL-6), interferon-γ (IFN-γ), and tumor necrosis factor-α (TNF-α), following PTT/CDT/immunotherapy treatment, suggesting effective activation of the immune response. The enhanced immunogenicity caused by AIT with αPD-1 treatment resulted in efficient antigen presentation, as indicated by the increased infiltration of dendritic cells (DCs) into the tumor-draining lymph nodes (LNs). We also observed enhanced infiltration of $CD8^+$ T cells in distant tumors in the AIT with αPD-1 group compared to αPD-1 alone. Hence, mitochondria-targeting represents an effective strategy to potentiate the combination of photothermal, chemodynamic, and immune checkpoint blockade therapies for the treatment of metastatic cancer.

1. Introduction

Cancer is a disease characterized by the uncontrolled growth of abnormal cells, which can spread locally or metastasize to distant parts of the body [1,2]. Common cancer treatments include surgery, chemotherapy and radiotherapy, with targeted therapy and immunotherapy also being employed when necessary [3–5]. Among these, immunotherapy has emerged as a powerful clinical tool for treating cancer by activating the immune system to eliminate tumor cells, thereby inhibiting cancer recurrence and metastasis [6,7].

Recently, immune checkpoint inhibitors (ICIs), targeting the programmed cell death protein 1 (PD-1)/programmed death-ligand 1 (PD-L1) axis and the cytotoxic T-lymphocyte-associated antigen-4 (CTLA-4) pathway, have achieved significant clinical advances, revolutionizing oncology treatments [8,9]. PD-L1, overexpressed on cancer cells, provides inhibitory signals to PD-1, which is expressed on activated T cells and transmits signals that counteract T-cell receptor activation [10,11]. Cancer cells exploit this immunosuppressive mechanism to evade immune destruction. Anti-PD-1 (αPD-1) therapy disrupts the PD-1/PD-L1 interaction, effectively reactivating T cells to target and kill cancer cells [12,13]. However, the response rate to ICB monotherapy remains low in clinical settings [14]. Therefore, exploring additional strategies to enhance its efficacy is imperative.

Photothermal therapy (PTT), a non-invasive treatment modality, has

* Corresponding author. Institute of Medical Technology, Peking University Health Science Center, Beijing, 100191, PR China.
E-mail address: lukuangda@hsc.pku.edu.cn (K. Lu).

https://doi.org/10.1016/j.mtbio.2025.101542
Received 2 December 2024; Received in revised form 28 January 2025; Accepted 1 February 2025
Available online 4 February 2025

been widely applied in localized cancer therapy [15–17]. Under near-infrared (NIR) light irradiation, photothermal agents (PTAs) in tumor tissues absorb laser energy, generating localized hyperthermia to ablate tumor cells [18,19]. Beyond its direct cytotoxic effects, PTT-induced thermal ablation also leads to tumor cell death, which releases tumor-associated antigens (TAAs) that can trigger an immune response to suppress tumor metastasis and recurrence [20,21]. However, the therapeutic efficacy of PTT alone is limited by the immunosuppressive tumor microenvironment and tumor heterogeneity.

Mitochondria play a crucial role in tumor growth, proliferation, invasion, and metastasis [22,23]. They are also recognized as key organelles responsible for generating damage-associated molecular patterns (DAMPs) [24–26]. Notably, mitochondria are highly sensitive to heat, and localized hyperthermia can cause substantial mitochondrial damage, leading to the release of DAMPs into the extracellular milieu. This process subsequently activates the immune system [27]. Based on this, we hypothesize that mitochondria-targeted PTT may not only cause more extensive cellular damage but also further enhance systemic immune activation.

Chemodynamic therapy (CDT) involves the conversion of endogenous hydrogen peroxide (H_2O_2) into highly cytotoxic hydroxyl radicals (•OH) through Fenton or Fenton-like reactions [28,29]. Iron or copper based nanocomposites (such as Fe_3O_4 and gold-copper nanoparticles) have been widely used in CDT due to their outstanding catalytic activities [30–32]. Notably, the generation of •OH is independent of O_2 and specifically utilizes the elevated H_2O_2 levels in tumor cells, making normal tissues less susceptible to CDT-induced damage [33,34]. The •OH radicals produced by the Fenton reaction effectively oxidize tumor cell membranes, proteins and DNA, inducing cell apoptosis and extensive tumor cell death. This process has been shown to exhibit features of immunogenic cell death (ICD) [35,36]. CDT-induced ICD can further stimulate dendritic cells (DCs) maturation, enhancing T cell infiltration into the tumor site and promoting effective immune activation [37,38]. Additionally, immune checkpoint inhibitors can synergistically enhance this process by reactivating T cells and preventing immune escape by tumor cells. The combination of CDT and immune checkpoint blockade presents a promising strategy for improving the outcomes of cancer therapy.

In this work, we developed a multifunctional AuCu alloy nanoparticle designed to target mitochondria for near-infrared (NIR)-triggered photothermal therapy (PTT) combined with chemodynamic therapy (CDT) to enhance cancer checkpoint blockade therapy. The

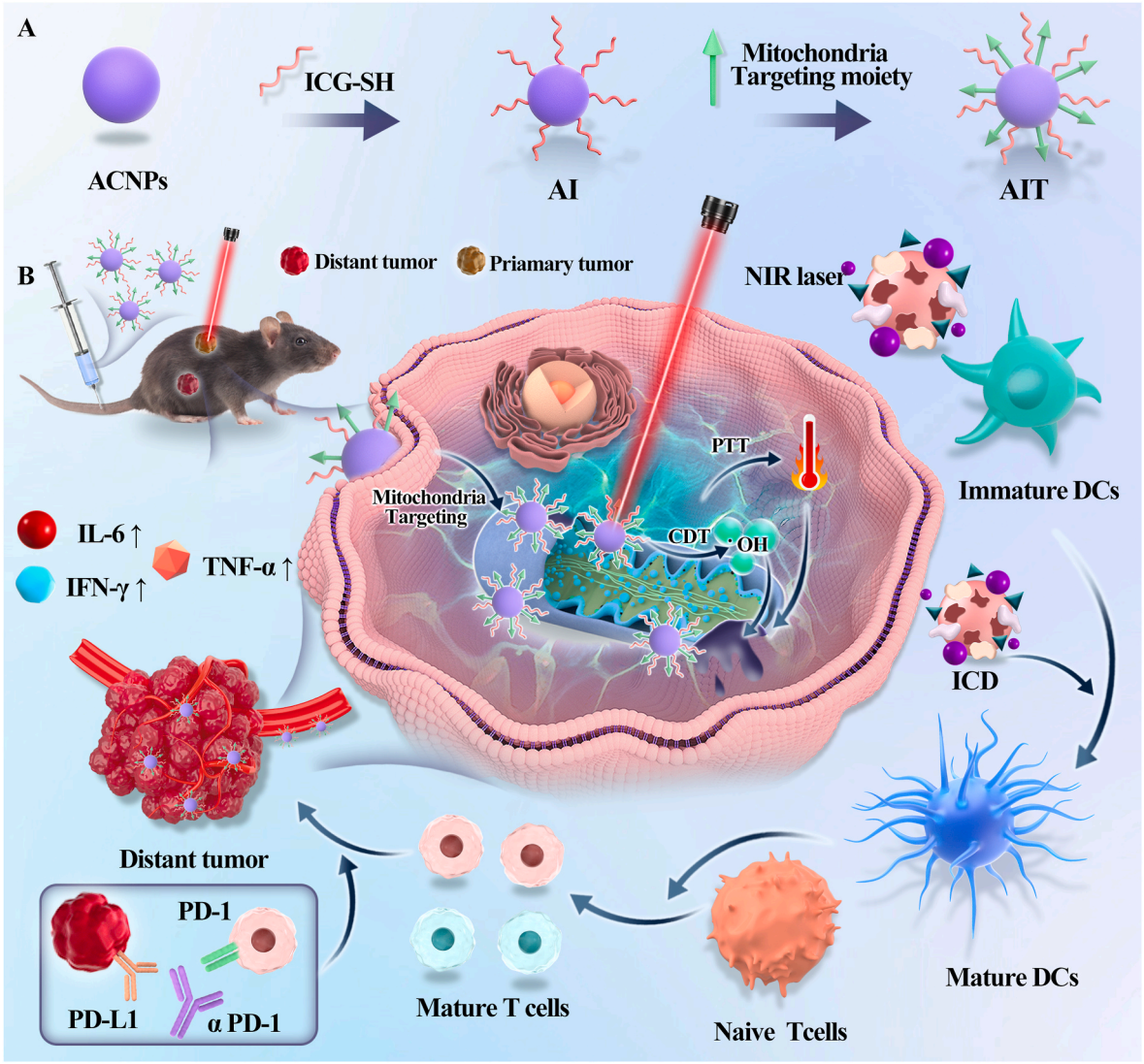

Scheme 1. Schematic illustration of AIT nanoparticles for mitochondria-targeted photothermal-chemodynamic therapy enhances checkpoint blockade immunotherapy. (a) The preparation of AIT NPs. (b) Schematic of AIT NPs for synergistic cancer therapy. The combination of ICB and ICD induced by PTT/CDT significantly promoted the antigen presentation and the infiltration of T cells, which inhibited the metastasis and recurrence of tumor cells.

gold-copper nanoparticles (AC NPs), coated with polyvinyl pyrrolidone (PVP), were functionalized with indocyanine green-thiol (ICG-SH) as a NIR photothermal agent and mercaptoethyl triphenylphosphonium (TPP-SH) as a mitochondria-targeting ligand. These engineered nanocarriers, termed AuCu-ICG-TPP (AIT), also harness the catalytic activity of Cu to decompose H_2O_2 into hydroxyl radicals through Fenton-like reactions. Upon NIR laser irradiation, AIT induces both photothermal and CDT-mediated damage, effectively provoking immunogenic cell death (ICD). When combined with a programmed cell death protein 1 (PD-1) antibody (αPD-1), this treatment strategy eradicates primary tumors while the release of tumor-associated antigens (TAAs) stimulates a robust systemic antitumor immune response. This immune activation triggers an abscopal effect, suppressing the growth of non-irradiated distant tumors, as demonstrated in the MC38 bilateral tumor model (Scheme 1). In summary, the AIT nanocarriers represent a novel therapeutic platform that leverages the synergistic effects of PTT/CDT and immunotherapy to enhance cancer treatment efficacy.

2. Materials and methods

2.1. Materials

$HAuCl_4{\cdot}3H_2O$ (99 %) and PVP K30 were bought from Shanghai Bide Pharmaceutical Technology Co., Ltd. $CuCl_2{\cdot}2H_2O$ and $NaBH_4$ were bought from Shanghai Macklin Biochemical Technology Co., Ltd. Indocyanine Green-Thiol (ICG-SH), Mercaptoethyl-triphenylphosphonium (TPP-SH) and Rhodamine B isothiocyanate thiol (RITC-SH) were bought from Xi 'an Haoran Biotechnology Co., LTD. Ascorbic acid (99.8 %) was purchased from Beijing Tongguang Fine Chemical Co. All reagents were of analytical grade and used without further purification.

2.2. Characterization

Transmission electron microscopy (TEM) images were captured using a JEM-1400 electron microscope. Dynamic light scattering (DLS) measurements were performed using Zetasizer NanoZS, Malvern Instruments. UV–vis absorption spectra were recorded using a double-beam UV–vis spectrophotometer (T3202S, Youke Instrucment, Shanghai). An 808 nm diode laser (Beijing Laserwave OptoElectronics Tech. Co. Ltd.) with tunable output power densities was employed to study the photothermal effect. Fluorescent images of MC38 cells were obtained by a Zeiss LSM 900 confocal laser scanning microscope. The Au concentration was assessed by PerkinElmer NexlON 350X inductively coupled plasma mass spectrometry (ICP-MS) measurements. Infrared thermal images were acquired by a Fluke infrared (IR) thermal camera. Flow cytometric analysis was conducted using the CytoFLEX nano flow cytometer (Beckman, USA).

2.3. Preparation of AC NPs

First, AuCu crystalline nucleus was prepared [39]. $NaBH_4$ (4 mg/mL, 0.6 mL) with 4 °C cold water was added into 3 mL of aqueous solution containing 2.06 mg $HAuCl_4{\cdot}3H_2O$ and 0.21 mg $CuCl_2{\cdot}2H_2O$, and the mixture was stirred for 30 min. Next, 50 μL of the aforementioned solution was added into 6 mL ethylene glycol/H_2O (5:1) solution with 100 mg PVP, 20 mg ascorbic acid, 5 mg $HAuCl_4{\cdot}3H_2O$ and 0.51 mg $CuCl_2{\cdot}2H_2O$. The solution was stirred at room temperature for 2 h. After that, AuCu nanoparticles were retrieved by ultrafiltration (Millipore, MWCO = 3 K) and washed three times with water.

2.4. Preparation of AuCu-ICG (AI)

ICG-SH methanol solution was added into an ACNP solution, and the mixture was stirred for 2 h to obtain AI. The AI nanoparticles were collected by centrifugation (15000 rpm, 30 min) and washed with methanol and ultrapure water.

2.5. Preparation of AuCu-TPP (AT)

TPP-SH aqueous solution was added into an ACNP solution, and the mixture was stirred for 2 h to obtain AT. The AT nanoparticles were collected by centrifugation (15000 rpm, 30 min) and washed twice with ultrapure water.

2.6. Preparation of AuCu-ICG-TPP (AIT)

First, ICG-SH was added to an ACNP solution, and the mixture was stirred for 2 h to obtain AI. The AI nanoparticles were washed twice with methanol and ultrapure water and collected by centrifugation (15000 rpm, 30 min). The AI nanoparticles were then dispersed in an aqueous solution. Subsequently, TPP-SH was added to the AI aqueous solution, and the mixture was stirred for 2 h. The solution was washed twice with water and collected by centrifugation (15000 rpm, 30 min) to obtain AIT.

2.7. Photothermal performance analysis of AIT

To investigate the photothermal performance of the as-synthesized AIT, an 808 nm NIR laser was delivered perpendicularly through 1.5 mL centrifuge tubes containing 0.5 mL of AIT aqueous dispersion at varying Au concentrations of 0, 12.5, 25, 50, 100 μg/mL, which corresponds to 0, 6.5, 13, 26, 52 μM of ICG. The NIR laser light source was set to 1 W/cm^2, and the illumination time was 10 min. Temperatures were recorded every 20 s using an infrared thermal camera (225S-L24, Fotric, China).

For photothermal stability tests, the aqueous solution of AIT (100 μg/mL) was exposed to 808 nm laser irradiation (1 W/cm^2) for 10 min. The laser was turned off for 10 min, and this on-off cycle was repeated six times. The solution temperature was recorded every 20 s.

The photothermal conversion efficiency was calculated based on a previous study [40].

2.8. Detection of ·OH generation in the aqueous solution

10 μL of AIT solution (1 mg/mL) or PBS solution and TMB solution (5 mM, 100 μL) were added to 0.89 mL of NaAc-HAc buffer (0.1 M, pH 4.5) containing 0.2 mM H_2O_2. The mixture was either irradiated or not irradiated with an 808 nm laser (1 W/cm^2, 10 min). After 30 min, the UV–vis absorption spectra at 652 nm were recorded to assess the catalytic oxidation of TMB.

2.9. Cell culture

The MC38 cells were purchased from Wuhan Pricella Biotechnology Co., Ltd. (Wuhan, China). The cells were cultured in high-glucose Dulbecco's Modified Eagle's Medium (DMEM) containing 10 % fetal bovine serum (FBS) and 1 % penicillin/streptomycin at 37 °C in a Forma 3111 CO_2 incubator (Massachusetts, USA) with 5 % CO_2.

2.10. Cellular uptake

The cellular uptake of AT, AI and AIT was estimated on MC38 cells. Using 6-well plates, cells were seeded at 1.0×10^6/well and cultured for 24 h. They were added to the cells at Au doses of 10 μg/mL. After incubation of 1, 3, 6, 12 and 24 h, the cells were washed three times with PBS to remove excess AC nanoparticles, then trypsinized and collected. And the cell numbers were counted by a hemocytometer. Cells were digested with lefort aqua regia and the Au concentrations were determined by ICP-MS (PerkinElmer, USA). Results are expressed as the amount of Au (ng) per 10^5 cells.

2.11. Co-localization study

MC38 cells were seeded in 35 mm laser confocal petri dishes and incubated at 37 °C with 5 % CO_2 for 24 h. Then the cells were incubated with PBS, RITC-labeled AI (AI-RITC) and AIT (AIT-RITC) with the Au doses of 10 μg/mL for different time (1, 3, 6, 12 and 24 h) and then rinsed three times with PBS to remove free nanoparticles. The cells were then incubated with MitoTracker Green solution (100 nM) at 37 °C for 30 min and stained with Hoechst 33342 for 20 min. Cells were washed three times with PBS and then 1 mL of PBS was added to the cells. Finally, the cells were imaged by confocal laser scanning microscope (CLSM).

2.12. Mitochondria isolation and ICP-MS analysis

Mitochondria from MC38 cells were isolated by a kit bought from MedChemExpress. Briefly, 2×10^7 cells were cultured in T175 and treated with 50 μg/mL AI, AIT and PBS for 12 h. Then 2×10^7 cells were collected by centrifugation. 1.5 mL of mitochondrial isolation reagent was added into the cell pellet and vortexed well. The cell suspension was put on the ice for 10 min. Next, the cell suspension was transferred to a cell homogenizer and ground. The mixture was centrifuged at 600 g for 10 min at 4 °C. Then the supernatant was transferred to a new tube and centrifuged at 11000 g for 10 min at 4 °C. Finally, the pellet was collected, and the amount of gold was measured using ICP-MS.

2.13. In vitro cell viability

MC38 cells were seeded in 96-well plates at 5000 cells per well which cultured at 37 °C with 5 % CO_2 for 24 h. Different concentrations (0, 100, 200, 300 and 400 μg/mL Au, corresponding to 0, 52, 104, 156, 208 μM ICG) of AT, AI and AIT dispersed in the culture media were added and co-incubated with the cells for 6 h. The cells were rinsed with PBS three times to clear away the remnant nanoparticles. Then irradiated with an 808 nm laser (1.0 W/cm^2, 10 min) or not. After 4 h, the cells were incubated with fresh medium containing 10 % cck-8 solutions (beyotime, China) for another 1 h. The absorbance of CCK-8 solutions in the cells were determined with a Microplate Reader (DeTie Biotechnology, China) at 450 nm.

2.14. Cytochrome c release

MC38 cells were seeded in 35 mm laser confocal petri dishes for 24 h and then treated with PBS, AT, AI or AIT at an equivalent dose of 300 μg/mL Au for 6 h. Cells were washed three times with PBS to remove the free nanoparticles, then irradiated by an 808 nm laser (1.0 W/cm^2, 10 min). After 4 h, cells were then stained with MitoTracker Red (Beyotime, China) at a concentration of 100 nM at 37 °C for 30 min. They were fixed with 4 % paraformaldehyde (PFA), blocked with 10 % BSA and then incubated with anti-cytochrome c antibody (Abcam, ab133504) overnight at 4 °C, followed by stained with Alexa Fluor®488-conjugated anti-rabbit secondary antibody (Abcam, ab150073) at room temperature for 2 h and Hoechst 33258 (Beyotime, China) for 20 min. Finally, the level of cytochrome *c* release was observed by CLSM.

2.15. Analysis of mitochondrial membrane potential (MMP)

1.0×10^5 MC38 cells were seeded in 35 mm confocal culture dishes and cultured for 24 h. Then the cells were incubated with PBS, AT, AI and AIT (300 μg/mL Au) for 6 h, followed by illumination for 10 min by 808 nm NIR light (1 W/cm^2). After 4 h of incubation, the cells were washed three times with PBS and stained with a JC-1 dye to measure the mitochondrial membrane potential according to the instructions. Finally, the fluorescence images of the cells was captured by CLSM.

2.16. Intracellular mitochondrial DNA (mtDNA) release experiment

To detect mtDNA, 1.0×10^5 MC38 cells were seeded in 35 mm confocal culture dishes and cultured overnight. Then the cells were incubated with PBS, AT, AI and AIT (300 μg/mL Au) for 6 h, followed by irradiation with an 808 nm NIR laser (1 W/cm^2) for 10 min. After another 4 h, cells were incubated with MitoTracker Red (100 nM) for 30 min at 37 °C. Subsequently, cells were fixed, permeabilized and blocked. Then the cells were incubated with anti-DNA antibody (Progen, AC-30-10) overnight at 4 °C, followed by staining with Alexa Fluor®488-conjugated anti-mouse secondary antibody (Abcam, ab150121) at room temperature for 2 h and Hoechst 33258 (Beyotime, China) for 20 min. Finally, images of cells were acquired by CLSM.

2.17. Ecto-calreticulin (CRT) staining on cell surface

MC38 cells were cultured in 35 mm laser confocal petri dishes for 24 h and then incubated with PBS, AT, AI or AIT at an equivalent dose of 300 μg/mL for 6 h. Cells were washed three times with PBS to remove the free nanoparticles, followed by exposure to 808 nm laser irradiation (1.0 W/cm^2, 10 min). After another 4 h incubated, the cells were fixed in 4 % paraformaldehyde, blocked with 10 % BSA, and then incubated with anti-calreticulin (Abcam, ab2907) antibody overnight at 4 °C. Subsequently, the cells were stained with Alexa Fluor®488-conjugated anti-rabbit secondary antibody (Abcam, ab150073) at room temperature for 2 h. After being washed three times with PBS, the nuclei were stained with Hoechst 33258 for 20 min at room temperature, finally the cells were imaged using CLSM.

2.18. HMGB1 staining in the nuclear of cell

MC38 cells were cultured in 35 mm laser confocal petri dishes for 24 h and then incubated with PBS, AT, AI, or AIT at an equivalent dose of 300 μg/mL for 6 h. Cells were washed three times with PBS to remove the free nanoparticles, followed by exposure to 808 nm laser irradiation (1.0 W/cm^2, 10 min). After 4 h, the cells were fixed in 4 % paraformaldehyde, blocked with 10 % BSA, and then incubated with anti-HMGB1 (Abcam, ab18256) antibody overnight at 4 °C. Subsequently, the cells were stained with Alexa Fluor®488-conjugated anti-rabbit secondary antibody (Abcam, ab150073) at room temperature for 1 h. After being washed three times with PBS, the nuclei were stained with Hoechst 33258 for 20 min at room temperature. Finally, the level of HMGB1 was measured using CLSM.

2.19. Apoptosis assay by flow cytometry

MC38 cells were seeded in six-well plates and incubated with high glucose complete DMEM (containing 10 % FBS) for 24 h. The cells were incubated with PBS, AT, AI or AIT at an equivalent dose of 300 μg/mL for 6 h. The medium was then removed, and the cells were washed three times with PBS to remove the free nanoparticles. Then the cells were irradiated with 808 nm NIR laser (1 W/cm^2) for 10 min or left untreated. The cells were further cultured for 4 h, detached using trypsin, and collected in 1.5 ml tubes. The subsequent steps followed the manufacturer's instructions for the Annexin V-FITC/PI apoptosis kit. Finally, the cells were resuspended in PBS and analyzed immediately using a flow cytometer (Beckman, USA). Unstained cells were used as negative controls.

2.20. Western blotting

MC38 cells (2×10^5) were cultured in six-well plates for 24 h and then treated with PBS, AT, AI or AIT at an equivalent Au dose of 300 μg/mL for 6 h, the cells were rinsed three times with PBS and followed by irradiation with 808 nm NIR laser (1 W/cm^2) for 10 min. After 4 h, cells were lysed and prepared for standard western blotting analysis. After

membrane transfer, anti-cleaved caspase-3 (Abcam, ab214430), anti-bcl-2 (Abcam, ab182858), beta actin (Proteintech, 66009-1-Ig), goat anti-mouse IgG secondary antibody HRP (Abcam, ab205719), and goat anti-rabbit IgG H&L (HRP) (Abcam, ab97051) were separately incubated with the cropped membranes for blotting.

2.21. Animal model

The C57BL/6N mice (5–6 weeks old, female) were purchased from Beijing Vital River Laboratory Animal Technology Co., Ltd. (China). All animal experiments were performed with the permission of the Animal Ethics Committee of Beijing Vital River Laboratory Animal Technology Co., Ltd. (China), according to the guidelines approved by Beijing Administration of Experimental Animals. The cell line MC38 (2×10^6 cells) in 100 μL PBS were injected subcutaneously to the right flank of C57BL/6N mice, When the tumor volume reached approximately 50–100 mm^3, the mice were deemed ready for experiments.

2.22. Photoacoustic imaging (PAI) performance of AIT

For *in vivo* PA imaging, the MC38 tumor–bearing C57BL/6N mice were anesthetized and monitored by a photoacoustic/ultrasonic multimodal small animal imaging system (Vevo 3100 LAZR, Canada). PA imaging was performed after the injection of AIT (10 mg Au/kg b.w.) at different time points (1, 6, 12, 24 and 48 h), with the PBS group serving as the control. The whole mouse was scanned with a step size of 0.30 mm. After data acquisition, the PA images were reconstructed using a standard back projection algorithm.

2.23. Evaluation of blood half-lives and biodistribution study of AIT

MC38 tumor-bearing mice (n = 3) were intravenously injected with 200 μL of AIT (10 mg Au/kg b.w.). Blood samples were collected from the angular vein at different time points (5 min, 30 min, 1 h, 3 h, 6 h, 12 h, 24 h, 48 h) after injection. At every time point, the mice were euthanized and tumors and the main organs (heart, liver, spleen, lung and kidneys) were acquired and weighed. All samples were treated by lefort aqua regia. The Au content of samples were determined by ICP-MS. Results are expressed as the %ID/g, which is calculated as the percentage of the element mass per gram of tissue to the total injected element mass.

By using Origin software, blood half-lives of AIT (in %ID/g) were fitted using two-compartment intravenous injection model.

2.24. In vivo antitumor efficacy

The Laboratory Animal Centre of Peking University performed the animals' experiments with an approval from Peking University. The mice were randomly divided into eight groups (n = 6 for each group) and treated with the following experimental conditions: (1) PBS (2) AT (3) AI (4) AIT (5) PBS+808 nm laser (6) AT+808 nm laser (7) AI+808 nm laser (8) AIT+808 nm laser. Different groups at an equivalent dose of 10 mg Au/kg b.w. or PBS were injected intravenously into MC38 bearing-tumor mice. Twelve hours post-injection, the mice were anesthetized, and their tumors were exposed to an 808 nm NIR laser (1 W/cm^2) for 10 min. After these operations, the tumor size was measured by a caliper every other day and calculated as volume = (tumor length) × (tumor width)^2/2. The body weights of the mice were also recorded, and the results were shown as a function of time. When the experiment reached the end, major organs (heart, liver, spleen, lung and kidneys) were excised and embedded in paraffin for hematoxylin−eosin staining (H&E). And tumors were weighted, photographed and collected for H&E, TUNEL, Ki-67, CRT and HMGB1 immunofluorescence staining.

2.25. Abscopal effect on bilateral tumor model

MC38 bilateral tumor models were established in C57BL/6N mice by subcutaneously inoculating 2×10^6 MC38 cells into the right flank (primary tumor) and 4×10^5 MC38 cells into the left flank (distant tumor). When the primary tumors reached approximately 100 mm^3, mice were randomly divided into four groups ($n = 6$): (1) PBS without irradiation as a negative control; (2) AIT plus αPD-1 without irradiation; (3) AIT with irradiation; (4) AIT with irradiation plus αPD-1. The treatments were administered intravenously at a dose of 10 mg Au/kg b.w., the primary tumors were irradiated with an 808 nm laser at 1.0 W/cm^2, and αPD-1 was intraperitoneally injected at a dose of 100 μg/mouse every two days for a total of two injections. Tumor volumes and body weights were measured every two days following treatment. When the primary tumor size of the PBS group reached 1000 mm^3, mice were sacrificed and both the primary and distant tumors were excised, weighed and photographed. And the blood was collected for the detection of related cytokines (Mouse interleukin 6 (IL-6), tumor necrosis factor α (TNF-α), and interferon γ (IFN-γ)).

2.26. Flow cytometry for immune response

Treated MC38 tumor-bearing C57BL/6N mice were scarified, distant tumors were collected and crushed, treated with a mixture of collagenase I and IV at a concentration of 2 mg/ml (Macklin, China) for 30 min at 37 °C, and ground with the rubber end of a syringe through 70 μm nylon mesh filters. Bilateral tumor-draining lymph nodes (LNs) were harvested and ground using 70 μm nylon mesh filters to obtain a single-cell suspension. Cells were then stained with the following fluorochrome-conjugated antibodies: CD45.2 (104.2), CD3ϵ (145-2C11), CD8α (53-6.7), CD11c (N418), CD86 (GL-1), CD80 (16-10A1) and examined by flow cytometry.

2.27. Statistical analysis

The error of the parallel test was calculated as mean ± SD. The data were analyzed by Origin software and the significant differences: *$p < 0.05$, **$p < 0.01$, ***$p < 0.001$. Statistical analyses were conducted using Origin (version 2023).

3. Results and discussion

3.1. Preparation and characterizations of AC-ICG-TPP (AIT)

The preparation of AuCu (AC) nanoparticles was described in the Experimental Section. Indocyanine green-thiol (ICG-SH) and mercaptoethyl-triphenylphosphonium (TPP-SH) were conjugated to AuCu in two steps via stable Au-S bonds to form AIT nanoparticles. For subsequent experiment, AC-TPP (AT) and AC-ICG (AI) nanoparticles were separately synthesized as controls. Transmission electron microscopy (TEM) showed that both AC and AIT were spherical with diameters of about 10 nm (Fig. 1a and S1). After dispersed in PBS for 24 h, the size and morphology of AIT remained unchanged, as observed through TEM images (Fig. S2), indicating that AIT is stable in a physiological environment. The hydrodynamic diameter of AC was 18 nm with a PDI of 0.30. After ICG and TPP loading, the hydrodynamic diameter of AIT increased to 72 nm with a PDI of 0.19 (Fig. S3). The zeta potential of AC nanoparticles decreased from −3.42 ± 0.43 mV to −16.70 ± 0.10 mV after ICG loading. Upon further coupling with TPP, the surface potential shifted from negative to positive, reaching 17.47 ± 0.51 mV (Fig. 1b), indicating successful loading of ICG and TPP. The ICG payload was quantified using UV–vis spectroscopy (absorption peaks at 785 nm) [41,42] by differential subtraction of the free ICG in the supernatant after centrifugation. The loading percentage of ICG in AIT was determined to be 30.51 % ± 2.66 %, based on the standard curve (Fig. S4). Meanwhile, the Au/Cu ratio in the AIT sample, as determined

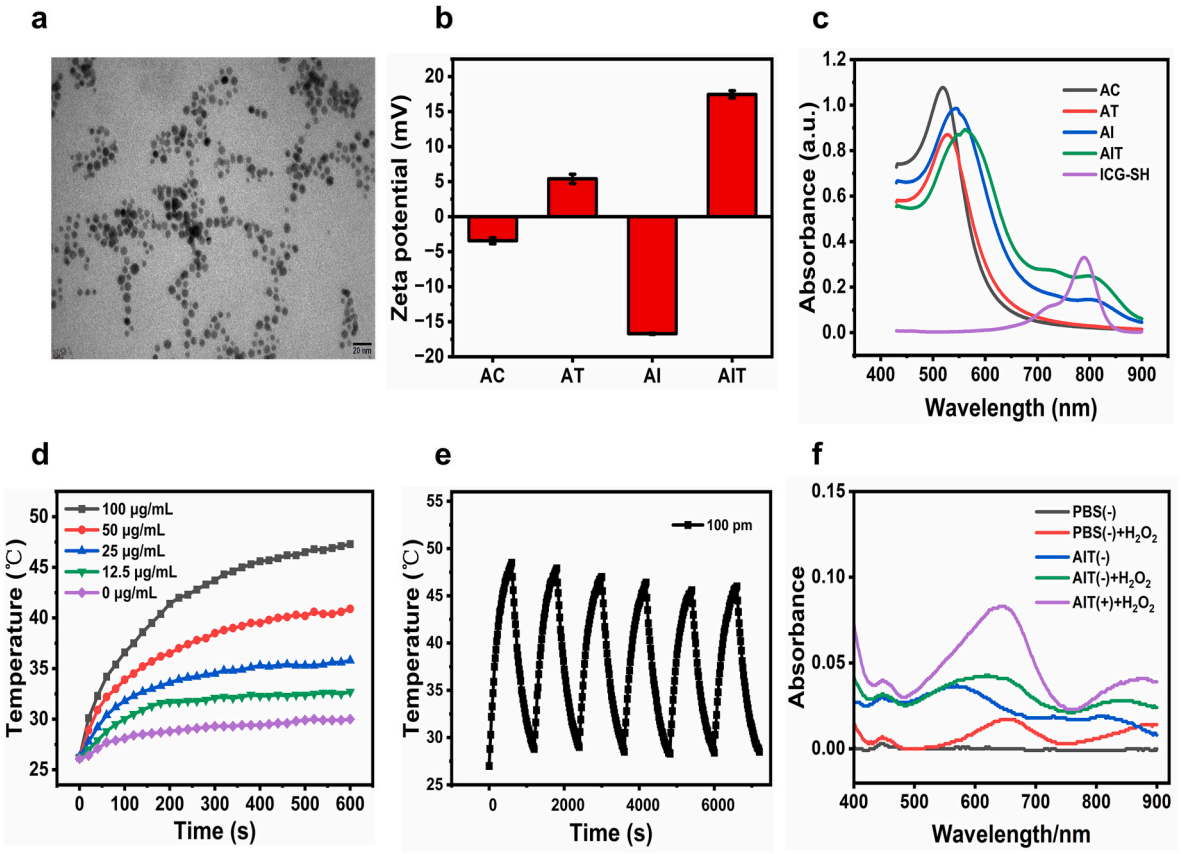

Fig. 1. (a) Transmission electron microscopy (TEM) pictures of AIT. Scale bar: 20 nm. (b) Zeta potential of AC, AT, AI and AIT. (c) UV/Vis absorption spectra of AC, AT (AC-TPP), AI (AC-ICG), AIT (AC-ICG-TPP) and ICG-SH. (d) Temperature variation curves of AIT at different particle concentrations (0, 12.5, 25, 50, 100 μg/mL by Au or 0, 6.5, 13, 26, 52 μM by ICG) under 808 nm laser (1.0 W/cm^2). (e) Temperature variations of an AIT solution (100 ppm of Au, corresponding to 52 μM ICG) over six cycles of heating and natural cooling. (f) ·OH generation by AIT detected through TMB method. (+) refers to NIR laser irradiation and (−) refers to dark.

by inductively coupled plasma mass spectrometry (ICP-MS), was 4:1, comparable to AC nanoparticles. UV–visible absorption spectroscopy showed that the absorption peak of ICG in both AI and AIT was red-shifted from 785 nm to 800 nm, which better matched the near-infrared laser source (808 nm) (Fig. 1c). These results confirm that ICG molecules were successfully conjugated to the surface of AC.

The photothermal performance is important for PTAs. When AIT was exposed to 808 nm laser irradiation (1 W/cm^2), the temperature of the solution rose. With the increase in particle concentration, both the heating rate and the final temperature also increased. The maximum temperature reached 47.3 °C after 10 min of irradiation (100 μg/mL by Au or 52 μM by ICG concentration, Fig. 1d). Moreover, we did not observe a significant decrease in temperature elevation after six irradiation/cooling cycles, indicating that the nanocarriers possessed good photostability (Fig. 1e and S5). The photothermal conversion efficiency (η) of AIT was calculated to be 30.3 % (Fig. S6). The catalytic production of ·OH by AIT in H_2O_2 was investigated using the 3,3′,5,5′-tetramethylbenzidine (TMB) assay. As shown in Fig. 1f, the characteristic peaks of TMB at 652 nm were observed in the AIT sample upon the addition of H_2O_2, compared to the AIT group without H_2O_2. Notably, the peak intensity significantly increased following NIR laser irradiation, demonstrating that PTT could further amplify the CDT effect.

3.2. *In vitro ROS generation and mitochondria-targeting ability*

In order to determine the appropriate incubation time for the cell experiments throughout the study, we first assessed the uptake of AIT by MC38 cells. As demonstrated in Fig. 2a, the cell uptake was almost complete after 6 h of incubation. Therefore, we incubated the cells with nanoparticles for 6 h in the following experiments unless otherwise stated.

The ROS production of different NPs in MC38 cells was also investigated using the intracellular ROS probe (DCFH-DA) and imaged with a confocal fluorescence microscope. Fluorescence images (Figs. S7 and S8) and quantitative analysis (Fig. 2b) revealed that the AI group without laser irradiation exhibited only weak fluorescence signals, whereas the AI with irradiation group displayed a moderate fluorescence signal, suggesting that the thermal effect facilitates the decomposition of AC to induce CDT. In contrast, the AT + laser group and all groups without NIR laser irradiation showed no detectable fluorescence signals, indicating that NIR light alone cannot activate AC to produce CDT. This also highlighted the low copper toxicity of our nanomaterials in the absence of NIR light. Notably, the AIT + laser group exhibited significantly higher levels of green fluorescence ($p < 0.01$) compared to the AI + laser group, likely due to the enhanced mitochondrial damage caused by AIT, which generated more ROS. These findings confirmed that mitochondria-targeting PTT effectively amplified the CDT effect.

To investigate the ability of AIT to target mitochondria *in vitro*, we incubated Rhodamine B-labeled AIT (AIT-RITC) with MC38 cells, while mitochondria were stained with MitoTracker Green. As shown in Fig. 2c and S9, the fluorescent signal of AIT-RITC fused well with mitochondria after 12 h of incubation (Pearson coefficient = 0.77). In contrast, there was no obvious co-localization between the fluorescence signals of AI-RITC and mitochondria (Pearson coefficient = 0.22). We further confirmed the locations of AIT by isolating mitochondria from MC38 cells using a mitochondria isolation kit. The mitochondrial suspension was treated with aqua regia, and the Au content of the isolated mitochondria was measured by ICP-MS (Fig. S10). The Au content in the AIT-

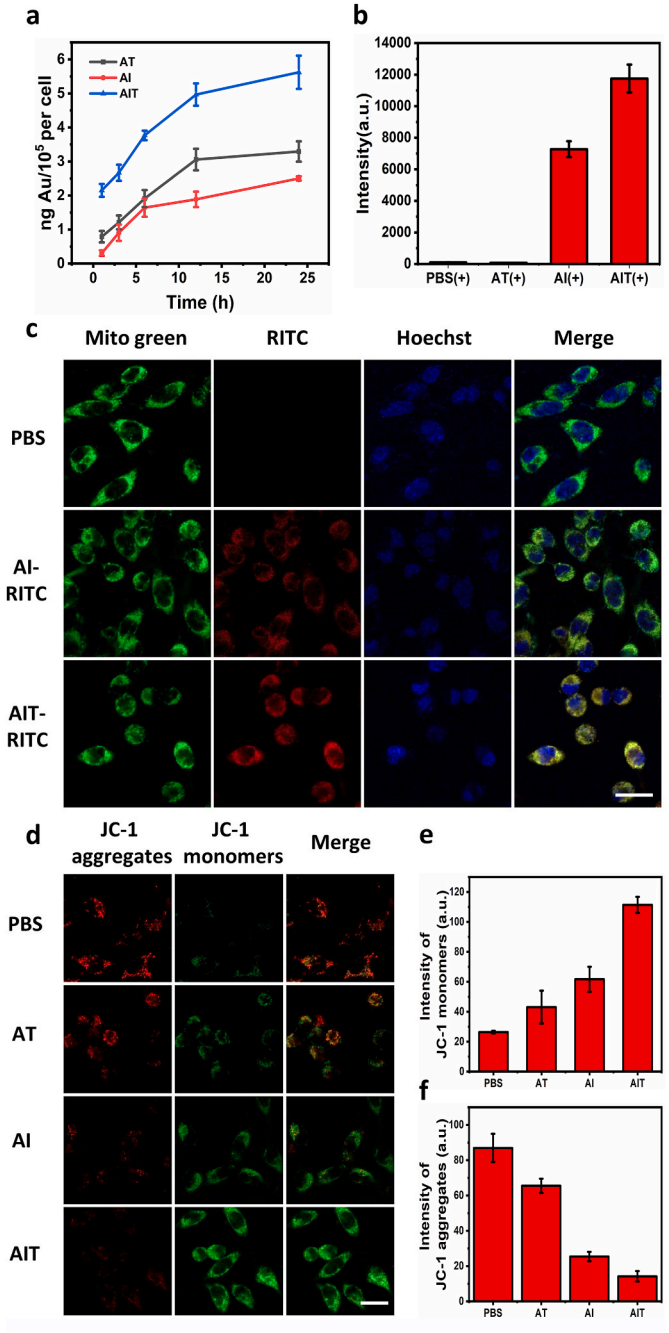

Fig. 2. (a) Cellular uptake amounts of AT, AI and AIT in MC38 cells at different incubation time. (b) Average cellular fluorescence signal of DCFH-DA indicating ROS production under 808 nm laser irradiation in each group. (c) CLSM images showing mitochondria co-localization in MC38 cells incubated with PBS, AI and AIT. Scale bar: 40 μm. (d) Intracellular MMP variation indicated by JC-1 after various treatments. Scale bar: 40 μm. (e) Average cellular fluorescence signal of JC-1 monomers in each group. (f) Average cellular fluorescence signal of JC-1 aggregates in each group.

treated group was 72.6 folds of that in the AI-treated group, indicating successful mitochondria targeting. To evaluate the enrichment of AIT in mitochondria over time, cells were incubated with AI-RITC and AIT-RITC for various durations. As shown in Figs. S11 and S12, mitochondrial co-localization in the AIT-RITC group increased over time, reaching a relatively high level at 6 h (Pearson coefficient = 0.67) and plateauing after 12 h (Pearson coefficient = 0.75). In contrast, mitochondrial co-localization in the AI-RITC group remained consistently low (Pearson coefficient = 0.21) even after 24 h of incubation. These findings demonstrated that AIT possessed high efficiency in targeting mitochondria.

The reduction of mitochondrial membrane potential (MMP) can be indicated by JC-1 assay. JC-1 typically aggregates around mitochondria, emitting red fluorescence in living cells. When mitochondrial membrane is disrupted, JC-1 shifts to the cytosol as monomers, emitting green fluorescence [43]. As demonstrated in Fig. 2d–f, the AIT + laser group showed weaker red fluorescence and stronger green fluorescence than the AI group and AT + laser group, which proved that the mitochondria-targeting strategy successfully enhanced mitochondrial membrane destruction by PTT/CDT.

3.3. Cell death mechanism and immunogenic cell death (ICD) analysis

To evaluate the *in vitro* killing effect of AIT, cell viability was assessed using the cell counting kit-8 (CCK-8) assay. The cytotoxicity of different samples at various concentrations (0, 100, 200, 300, 400 μg/mL by Au or 0, 52, 104, 156, 208 μM by ICG) in the dark or with irradiation was studied. All groups showed low cytotoxicity in the dark, even when the concentration reached 400 μg Au/mL (Fig. S13). After NIR laser irradiation, the viability of MC38 cells decreased with increasing incubation concentration. The AI group had a more significant killing effect on cells ($p < 0.001$) compared with the AT group, especially at high concentrations, which indicated that PTT damaged tumor cells. Meanwhile, the cell viability of the AIT group (25.46 %) was significantly lower than that of the AI group (51.84 %) at 400 μg Au/mL ($p < 0.001$), suggesting that mitochondria-targeted PTT was more effective than PTT alone in ablating tumor cells (Fig. 3a).

Flow cytometry experiments with Annexin V-FITC/PI (Fluorescein Isothiocyanate/Propidium Iodide) double staining were performed to examine the apoptosis ratio of MC38 cells after incubation with AIT under 808 nm NIR laser irradiation. MC38 cells treated with different nanoparticles without 808 nm laser irradiation showed few apoptotic and dead cells. However, after exposure to irradiation, the ratio of total apoptotic cells (both early and late stage) in the AI group was 14.83 %, significantly higher than that in the PBS and AT groups (5.04 % and 7.47 %, respectively). The ratio of total apoptotic cells treated with AIT reached 75.81 %, with the proportion of late apoptotic cells at 46.27 % (Fig. 3b), indicating that mitochondria targeting further enhanced the killing effect of PTT/CDT on tumor cells.

The release of cytochrome *c* (cyt *c*) into the cytoplasm, caused by mitochondrial dysfunction, is one of the key factors in cell apoptosis [44]. It binds to Apaf-1, an activator of apoptotic protein, to activate caspase 9 and downstream related proteins, which are key components in the execution of apoptosis. Hence, the release of cytochrome *c* is a good indicator of mitochondria-associated apoptosis [45]. As shown in Fig. 3c, we observed the most notable fluorescence separation of cyt *c* and mitochondria in the AIT group compared with others, suggesting that AIT induces more mitochondria-associated apoptosis. The Pearson coefficients for the PBS, AI, AT, and AIT groups were 0.81, 0.79, 0.69 and 0.60, respectively (Fig. 3d and S14).

We further investigated the cell death mechanism by examining the associated cell apoptosis pathways. Bcl-2 inhibition and caspase-3 cleavage are characteristic features of apoptosis [46,47]. We assessed Bcl-2 and cleaved caspase-3 levels after NIR laser irradiation by western blotting (WB). As shown in Fig. 3e and S15, cells treated with AIT exhibited the most significant downregulation of Bcl-2 proteins, accompanied by the highest levels of cleaved caspase-3. These findings confirmed the activation of the mitochondrial apoptotic pathway following mitochondria-targeted PTT/CDT.

It has been reported that PTT and CDT can induce an anticancer immune response [48,49]. We propose that AIT-mediated PTT/CDT synergistic therapy could also evoke the ICD of tumor cells. Calreticulin (CRT) in the endoplasmic reticulum is a sign of "eat me" [50]. When transferred to the surface of damaged cancer cells, it can be recognized

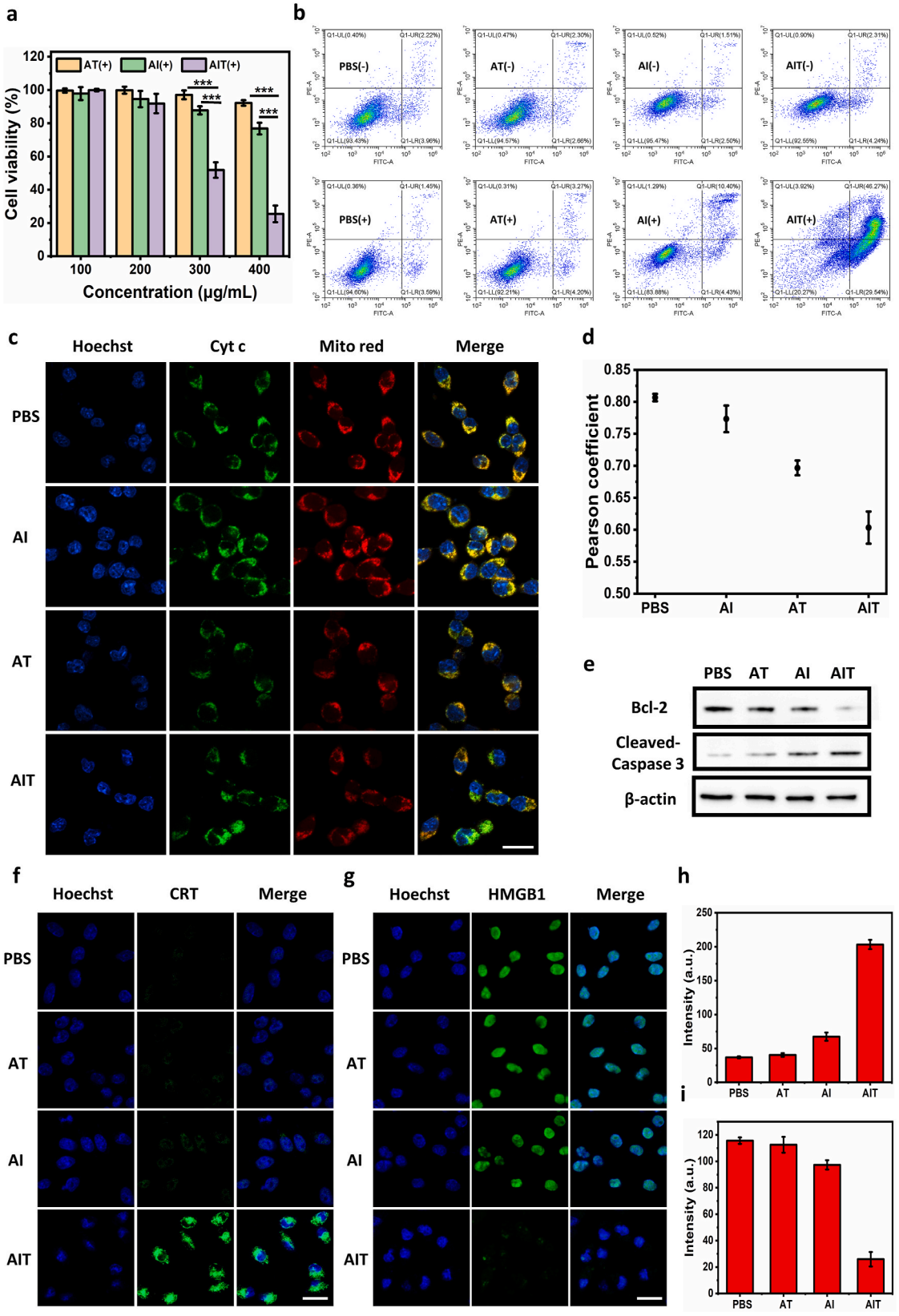

Fig. 3. (a) Cell viabilities of MC38 cells incubated with AT, AI and AIT at different concentrations under 808 nm laser irradiation. (b) Flow cytometry analysis showing apoptosis after various treatments. (+) refers to 808 nm laser irradiation. (c) CLSM images showing Cyto c release. Scale bar: 40 μm. (d) Pearson correlation analysis indicating the co-localization of mitochondria and Cyto c in different samples. (e) Variations in the levels of cleaved caspase-3 and bcl-2 in different groups by Western blots. (f) Immunofluorescence staining showing CRT exposure on MC38 cells after various treatments. Scale bar: 40 μm. (g) Immunofluorescence staining of HMGB1 in the nucleus after various treatments. Scale bar: 40 μm. (h) Quantitative analysis of the level of CRT (i) Quantitative analysis of the level of intranuclear HMGB1. *$p < 0.05$, **$p < 0.01$, ***$p < 0.001$.

by antigen-presenting cells (APCs), further inducing the cytotoxicity of T lymphocytes. After incubation with different nanomaterials, the expression of CRT on the surface of MC38 cell was imaged by immunofluorescence staining. Cells treated with AIT showed strong green fluorescence representing CRT (Fig. 3f), which was 5.51/3.02 times higher relative to that in cells treated with PBS/AI (Fig. 3h), proving that mitochondria-targeted PTT/CDT could significantly improve CRT exposure. High mobility group box 1 (HMGB1), another ICD biomarker, is primarily present in the nucleus and is released into extracellular space during cell necrosis, further activating the innate immune system and recruiting inflammatory cells, which plays a role in signaling in various immune cells [51]. As shown in Fig. 3g, after NIR laser irradiation, the fluorescence intensity of HMGB1 in the nucleus was reduced by 4.46 times in the AIT group compared with the PBS group. Interestingly, the fluorescence intensity of HMGB1 did not significantly decrease after AI treatment, indicating the importance of mitochondrial targeting in this process (Fig. 3i). As previously reported, changes in mitochondrial permeability (such as apoptosis due to mitochondrial damage) facilitate the release of damaged mitochondrial DNA (mtDNA) into the cytoplasm, further promoting the activation of immune effects [52–54]. After AIT + laser treatment, double-stranded DNA (dsDNA) signal in the cytosol, outside of the mitochondria, was more prominent in the cells. Notably, this phenomenon was not apparent in the other control groups (Fig. S16), suggesting that mitochondria-targeted photothermal therapy could better promote the release of mtDNA. In conclusion, mitochondria-targeted PTT/CDT induces strong ICD, which may further trigger a systemic antitumor immune response.

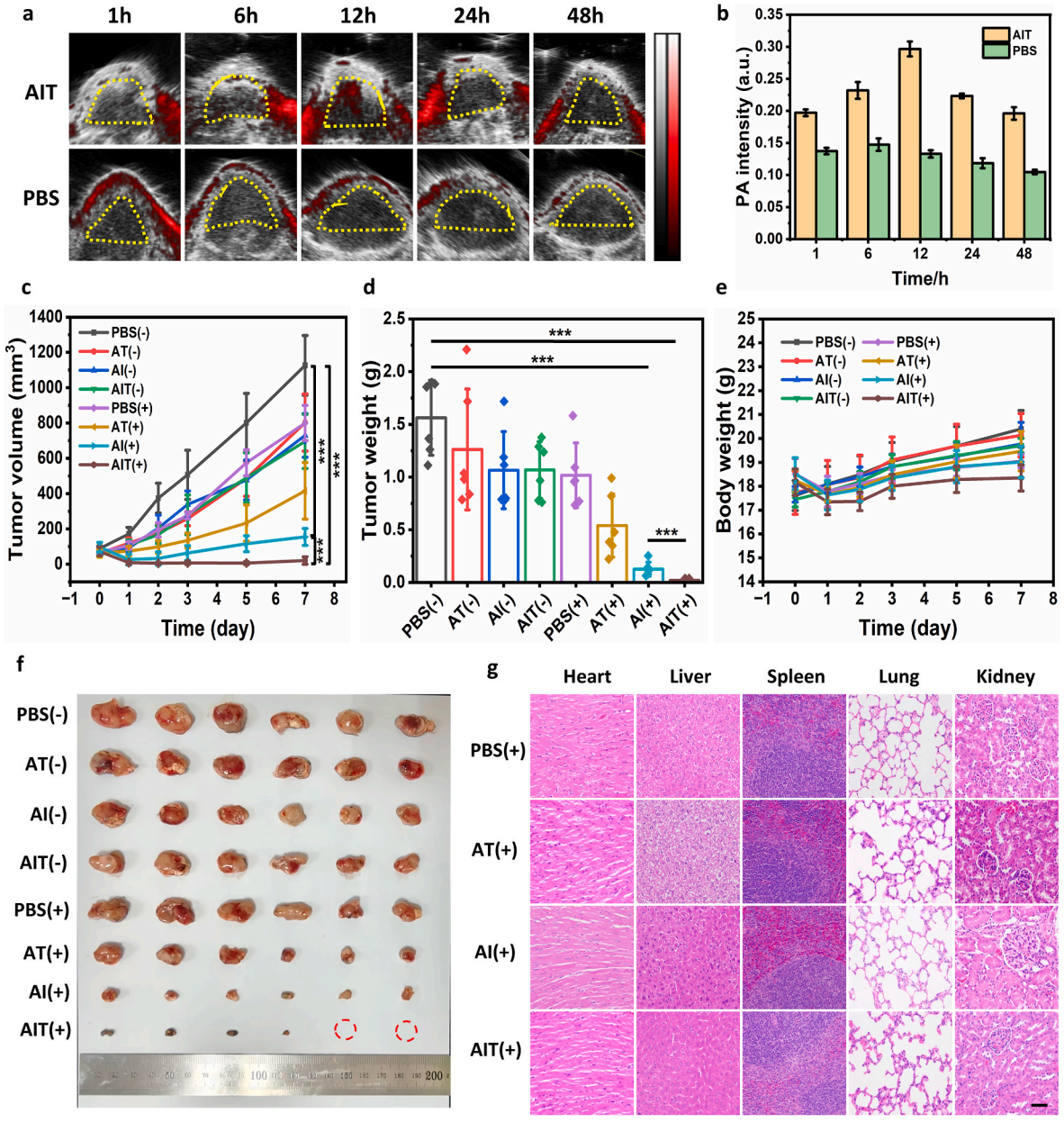

Fig. 4. (a) PA imaging showing AIT accumulation over time in mice tumor. The dashed area corresponds to the tumor site. (b) Relative PA intensities in the tumor region. (c) Tumor growth curves of MC38 tumor-bearing mice treated with PBS, AT, AI or AIT with (+) or without (−) NIR laser irradiation. (d) Average weights of excised tumors at the end point. (e) Body weights of mice after various treatments. (f) Photographs of the collected tumors after treatments. (g) H&E-stained slice pictures of heart, liver, spleen, lung and kidney, scale bar: 50 μm *p < 0.05, **p < 0.01, and ***p < 0.001.

3.4. In vivo pharmacokinetic and photoacoustic imaging of AIT

To evaluate the pharmacokinetics and biodistribution of AIT, an MC38 tumor-bearing mouse model was established. An equivalent dose of 10 mg/kg of AIT was injected into the mice via the tail vein. The AIT concentrations in the blood and major organs were measured by ICP-MS. Fig. S17a suggests that the blood distribution half-life ($t_{1/2\alpha}$) and the elimination half-life ($t_{1/2\beta}$) of AIT were 0.2 h and 2.3 h, respectively. Biodistribution results indicated that there was almost no accumulation in the lungs, heart, and kidneys. AIT could also accumulate at the tumor site and reached a maximum concentration at 12 h (2.0 % ID/g), in addition to the liver, spleen, and lungs, which provided a reference for choosing the optimal treatment time for subsequent experiments (Fig. S17b).

Photoacoustic Imaging (PAI) is a non-invasive biomedical imaging method developed in recent years. The good photothermal properties and excellent photostability of AIT make it a promising platform for PAI. AIT was injected into the tumor-bearing mice via the tail vein at a dose of 10 mg/kg b.w. for PAI at different time points, with PBS used as a negative control. As shown in Fig. 4a and b, the acoustic signals at the tumor site reached a maximum at 12 h, which was consistent with the biodistribution data. Hence, it is clear that AIT can provide exceptional acoustic contrast for tumor diagnosis.

3.5. In vivo antitumor efficacy

An MC38 subcutaneous transplantation tumor mouse model was established to study the tumor-killing effect of AIT *in vivo*. When the tumors reached approximately 50–100 mm^3 in volume, PBS, AT, AI, and AIT were injected at a dose of 10 mg Au/kg b.w. into each mouse via the tail vein. Twelve hours after injection, the tumors were irradiated with 808 nm NIR laser (1 W/cm^2) for 10 min, or not irradiated. As shown in Fig. 4c and f, the AIT group with NIR irradiation effectively destroyed the tumor. In two of the six mice, the tumors were cured. At the end of the experiment, the tumor sizes in the AIT with NIR laser group were as low as 1.81 % of those in the PBS untreated group. AI/AT with NIR laser treatment could also inhibit tumor growth (tumor sizes were only 13.73 % and 36.94 % of the PBS untreated group, respectively), but were less potent compared to AIT. In addition, all groups in the dark and PBS with NIR laser irradiation couldn't inhibit tumor growth. The tumor weights in the AIT group were the lowest compared to the PBS and AI groups ($p < 0.001$, Fig. 4d).

Tumor tissue slices from different groups were collected from sacrificed mice for further HE staining, TUNEL, and Ki-67 immunofluorescence staining (Fig. S18). The images of HE-stained slices showed that the tumor tissue was greatly destroyed by AI/AIT with NIR irradiation, while the other groups still showed infiltration and distinguishing characteristics of tumor tissue. The AIT with NIR treatment group exhibited significantly higher fluorescence from TUNEL staining than the control groups, suggesting the efficient therapeutic effect on cancer cell apoptosis. Meanwhile, Ki-67 immunofluorescence staining was used to examine the proliferation capacity of tumors. The AIT with NIR treatment group showed no obvious red fluorescence signal compared to the control groups with high fluorescence, indicating that it significantly inhibited tumor cell proliferation. The expression levels of representative ICD markers in tumor tissues, including the cell surface exposure of CRT and HMGB1 in the nucleus, were also investigated. The AIT group with NIR laser irradiation had the most distinct exposure of CRT and the release of HMGB1, which further verified that mitochondria-targeted PTT/CDT synergistic therapy could activate the immune response at the tumor site. Moreover, both the body weight and histological analysis of major organs in mice, with or without NIR laser irradiation, did not show any significant changes among all groups (Fig. 4e–g, and S19), proving the great biocompatibility of these nanodrugs. In addition, no significant abnormalities were observed in the behavior of all the mice, demonstrating the non-toxicity of AIT treatment.

3.6. Antitumor abscopal effect and immune response activation

To explore whether the immune response provoked in the primary tumor was powerful enough to clear residual primary tumor tissue and inhibit untreated distant tumors, bilateral syngeneic MC38 tumor models were established. Different nanoparticles were injected intravenously, and the primary tumors were irradiated with 808 nm NIR laser (or not) 12 h after injection, while the distant tumors were protected from irradiation (Fig. 5a). As shown in Fig. 5b–d, the primary tumors in the AIT and AIT plus αPD-1 groups were eradicated after irradiation, which again indicated that mitochondria-targeted PTT/CDT possessed the capability to efficiently eradicate tumor tissues in situ. Alternatively, αPD-1 alone had almost no inhibitory effect on the primary tumor, likely due to the suppressive microenvironment.

For the distant tumors, AIT plus αPD-1 with irradiation successfully suppressed tumor growth. The volume and weight were only 108.64 ± 116.68 mm^3 and 72.07 ± 104.28 mg, which represented 84.15 % and 79.47 % reduction compared with the PBS group, respectively (Fig. 5e–g). AIT with irradiation showed limited inhibition (418.94 mm^3) on distant tumors, possibly due to the weak immune response stimulated by primary tumor destruction. Partial inhibition of the distant tumors was also observed in mice treated with αPD-1 alone (452.30 mm^3). In conclusion, the ICD induced by PTT/CDT synergizes with immune checkpoint blockade to elicit a strong systemic immune response and induces a significant abscopal effect. During the experiment, the weights of the mice were stable in all groups (Fig. S20). Moreover, H&E staining of the major organs further proved that none of the organs showed significant physiological lesions, suggesting that AIT combined with immune checkpoint therapy had good biosafety (Fig. S21).

A successful anti-tumor immune response depends on the efficient cooperation of the entire immune system. Markedly higher serum levels of pro-inflammatory factors, including IFN-γ, TNF-α, and IL-6, were found in mice treated with AIT with 808 nm laser plus αPD-1 compared with the PBS group (Fig. 5h–j). Meanwhile, the levels of these pro-inflammatory factors also increased to some extent in the AIT with NIR laser treatment group, demonstrating that AIT-mediated mitochondria-targeted PTT/CDT resulted in a moderate inflammatory response, which was a vital mechanism to initiate the immune response.

To further demonstrate the activation of antitumor immunity by AIT-enhanced immunotherapy, we studied the activity of antigen-presenting cells (APCs) in tumor-draining lymph nodes (LNs) after treatment. Dendritic cells (DCs), as the most established APCs, have a powerful ability to process antigens and present them to T cells in the LNs to elicit antitumor immunity [55,56]. We detected enhanced infiltration of DCs in the tumor-draining LNs in the AIT with irradiation plus *α*PD-1 group, facilitating sufficient antigen capture and presentation (Fig. 5k and S22a). Meanwhile, mature DCs should express characteristic surface markers (CD80/CD86) on their cell surfaces to activate subsequent T-cell responses. The proportion of $CD11c^+$ $CD80^+$ $CD86^+$ cells in the tumor-draining LNs was significantly improved in mice treated with AIT with NIR irradiation plus *α*PD-1 ($p < 0.001$, comparing to PBS groups), indicating the maturation of DCs (Fig. 5l and S22b). In AIT with NIR irradiation group, the proportion of recruited and matured DCs also increased ($p < 0.001$, comparing to PBS groups), confirming our hypothesis.

After antigen presentation, the infiltration of maturated T cells is cruial for tumor killing [57–59]. To detect whether AIT with irradiation plus *α*PD-1 increased T cell infiltration, the relative abundance of T cells in the LNs and tumors was measured. The relative abundance of $CD8^+$ T cells was substantially increased in the tumor-draining LNs after treatment with AIT with irradiation plus *α*PD-1 (Fig. 5m and S22c), likely recruited by maturated DCs. Moreover, the distant tumors in the AIT with irradiation plus *α*PD-1 treatment groups had noticeably higher $CD8^+$ T cell infiltration ($p < 0.001$, compared with PBS group, Fig. 5n and S22d), which could be attributed to the checkpoint blockade by

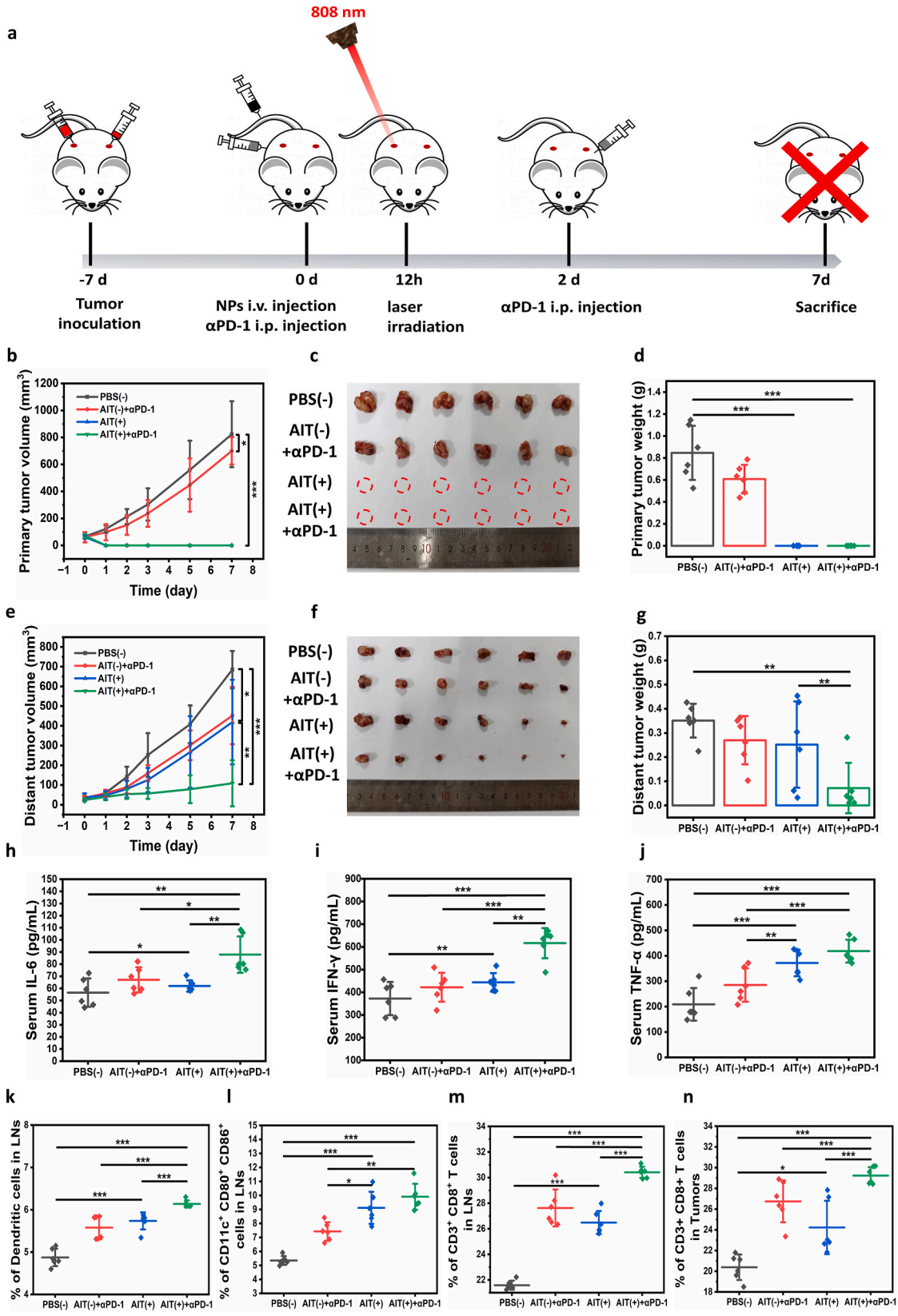

Fig. 5. (a) Schematic illustration of animal experimental design. (b) Growth curves of the primary tumors in the MC38 bilateral models. Photographs (c) and weights (d) of excised primary tumors at day 7 post-treatment. (e) Growth curves of distant tumors. Photographs (f) and weights (g) of excised distant tumors at day 7 post-treatment. The serum levels of IL-6 (h), IFN-γ (i), and TNF-α (j) after treatments (n = 6). The percentages of DCs (k), mature DCs ($CD11c^+CD80^+CD86^+$, l) and $CD3^+CD8^+$ T cells (m) in the tumor-draining LNs after treatments (n = 6). (n) The percentages of $CD3^+CD8^+$ T cells in distant tumors after treatments (n = 6). *p < 0.05, **p < 0.01, and ***p < 0.001.

αPD-1. Consistent with this, we also observed a significant increase of $CD8^+$ T cell infiltration in αPD-1 alone group.

All these results proved that AIT with irradiation could enhance the maturation of DCs through ICD effects, combining with facilitated T cell infiltration by checkpoint blockade, thus arousing a vigorous anti-tumor immune response.

4. Conclusion

To sum up, we developed a multifunctional nanoparticle, AIT, which enables mitochondrial-targeted PTT/CDT, combined with checkpoint blockade immunotherapy to treat metastatic cancer. Mitochondria targeting effectively enhanced ICD caused by PTT and CDT, leading to the release of tumor-derived proteins and subsequent DCs recruitment and maturation. Meanwhile, αPD-1 was employed to relieve the immunosuppression and promote T cell infiltration. Hence, mitochondria-targeted PTT/CDT synergize with checkpoint blockade immunotherapy to cure primary tumors and elicit a systemic immune response to inhibit distant tumors.

CRediT authorship contribution statement

Benchao Zheng: Writing – original draft, Software, Project administration, Investigation, Formal analysis, Data curation. **Hongbo Wang:** Methodology, Data curation. **Shiyi Zhai:** Methodology, Formal analysis. **Jiangsheng Li:** Methodology, Conceptualization. **Kuangda Lu:** Writing – review & editing, Supervision, Resources, Project administration, Funding acquisition, Conceptualization.

Declaration of competing interest

The authors declare that they have no known competing financial interests or personal relationships that could have appeared to influence the work reported in this paper.

Acknowledgements

We acknowledge Regional Innovation and Development Joint Fund of National Natural Science Foundation of China (U20A20384) and Clinical Medicine Plus X - Young Scholars Project, Peking University, the Fundamental Research Funds for the Central Universities (PKU2023LCXQ020).

Appendix A. Supplementary data

Supplementary data to this article can be found online at https://doi.org/10.1016/j.mtbio.2025.101542.

Data availability

Data will be made available on request.

References

[1] M.S. Hossain, H. Karuniawati, A.A. Jairoun, Z. Urbi, D.J. Ooi, A. John, Y.C. Lim, K. M.K. Kibria, A.K.M. Mohiuddin, L.C. Ming, K.W. Goh, M.A. Hadi, Colorectal cancer: a review of carcinogenesis, global epidemiology, current challenges, risk factors, preventive and treatment strategies, Cancers 14 (7) (2022) 1732.
[2] A. Leiter, R.R. Veluswamy, J.P. Wisnivesky, The global burden of lung cancer: current status and future trends, Nat. Rev. Clin. Oncol. 20 (9) (2023) 624–639.
[3] E. Fokas, A. Appelt, R. Glynne-Jones, G. Beets, R. Perez, J. Garcia-Aguilar, E. Rullier, J.J. Smith, C. Marijnen, F.P. Peters, M. Van Der Valk, R. Beets-Tan, A. S. Myint, J.-P. Gerard, S.P. Bach, M. Ghadimi, R.D. Hofheinz, K. Bujko, C. Gani, K. Haustermans, B.D. Minsky, E. Ludmir, N.P. West, M.A. Gambacorta, V. Valentini, M. Buyse, A.G. Renehan, A. Gilbert, D. Sebag-Montefiore, C. Rödel, International consensus recommendations on key outcome measures for organ preservation after (chemo)radiotherapy in patients with rectal cancer, Nat. Rev. Clin. Oncol. 18 (12) (2021) 805–816.
[4] Y. Kakeji, T. Oshikiri, G. Takiguchi, S. Kanaji, T. Matsuda, T. Nakamura, S. Suzuki, Multimodality approaches to control esophageal cancer: development of chemoradiotherapy, chemotherapy, and immunotherapy, Esophagus 18 (1) (2021) 25–32.
[5] X. Qu, D. Zhou, J. Lu, D. Qin, J. Zhou, H.-J. Liu, Cancer nanomedicine in preoperative therapeutics: nanotechnology-enabled neoadjuvant chemotherapy, radiotherapy, immunotherapy, and phototherapy, Bioact. Mater. 24 (2023) 136–152.
[6] B. Sangro, P. Sarobe, S. Hervás-Stubbs, I. Melero, Advances in immunotherapy for hepatocellular carcinoma, Nat. Rev. Gastroenterol. Hepatol. 18 (8) (2021) 525–543.
[7] C. Liu, M. Yang, D. Zhang, M. Chen, D. Zhu, Clinical cancer immunotherapy: current progress and prospects, Front. Immunol. 13 (2022) 961805.
[8] M.Z. Wojtukiewicz, M.M. Rek, K. Karpowicz, M. Górska, B. Polityńska, A. M. Wojtukiewicz, M. Moniuszko, P. Radziwon, S.C. Tucker, K.V. Honn, Inhibitors of immune checkpoints—PD-1, PD-L1, CTLA-4—new opportunities for cancer patients and a new challenge for internists and general practitioners, Cancer Metastasis Rev. 40 (3) (2021) 949–982.
[9] H. Zhang, Z. Dai, W. Wu, Z. Wang, N. Zhang, L. Zhang, W.-J. Zeng, Z. Liu, Q. Cheng, Regulatory mechanisms of immune checkpoints PD-L1 and CTLA-4 in cancer, J. Exp. Clin. Cancer Res. 40 (1) (2021) 184.
[10] M. Jalili-Nik, A. Soltani, B. Mashkani, H. Rafatpanah, S.I. Hashemy, PD-1 and PD-L1 inhibitors foster the progression of adult T-cell Leukemia/Lymphoma, Int. Immunopharmacol. 98 (2021) 107870.
[11] R. Makuku, N. Khalili, S. Razi, M. Keshavarz-Fathi, N. Rezaei, Current and future perspectives of PD-1/PDL-1 blockade in cancer immunotherapy, J Immunol Res 2021 (1) (2021) 6661406.
[12] M. Cevik, E. Namal, U. Iner-Koksal, N. Dinc-Sener, A. Karaalp, C. Ciftci, B. Susleyici, Association of PD-1 and PDL-1 gene polymorphisms with colorectal cancer risk and prognosis, Mol. Biol. Rep. 49 (3) (2022) 1827–1836.
[13] W. Piao, L. Li, V. Saxena, J. Iyyathurai, R. Lakhan, Y. Zhang, I.T. Lape, C. Paluskievicz, K.L. Hippen, Y. Lee, E. Silverman, M.W. Shirkey, L.V. Riella, B. R. Blazar, J.S. Bromberg, PD-L1 signaling selectively regulates T cell lymphatic transendothelial migration, Nat. Commun. 13 (1) (2022) 2176.
[14] P. Liu, L. Zhao, J. Pol, S. Levesque, A. Petrazzuolo, C. Pfirschke, C. Engblom, S. Rickelt, T. Yamazaki, K. Iribarren, L. Senovilla, L. Bezu, E. Vacchelli, V. Sica, A. Melis, T. Martin, L. Xia, H. Yang, Q. Li, J. Chen, S. Durand, F. Aprahamian, D. Lefevre, S. Broutin, A. Paci, A. Bongers, V. Minard-Colin, E. Tartour, L. Zitvogel, L. Apetoh, Y. Ma, M.J. Pittet, O. Kepp, G. Kroemer, Crizotinib-induced immunogenic cell death in non-small cell lung cancer, Nat. Commun. 10 (1) (2019) 1486.
[15] Y. Li, Y. Ding, Y. Zhang, Z. Sun, J. Liu, M. Dai, J. Feng, B. Li, C. Wang, Y. Wei, J.-W. Shen, An engineered cascade-sensitized red-emitting upconversion nanoplatform with a tandem hydrophobic hydration-shell and metal-phenolic network decoration for single 808 nm triggered simultaneous tumor PDT and PTT enhanced CDT, Nanoscale 15 (23) (2023) 10067–10078.
[16] T. Sun, H. Liu, N. Jiang, Q. Wu, C. Li, R. Xia, B. Gao, Z. Xie, Unadulterated organic nanoparticles with small sizes for robust tumor imaging and photothermal treatment, Adv. Funct. Mater. 31 (35) (2021) 2103714.
[17] W. Yang, N. Wang, J. Yang, C. Liu, S. Ma, X. Wang, W. Li, M. Shen, Q. Wu, C. Gong, A multifunctional 'golden cicada' nanoplatform breaks the thermoresistance barrier to launch cascade augmented synergistic effects of photothermal/gene therapy, J. Nanobiotechnol. 21 (1) (2023) 228.
[18] W. Shao, C. Yang, F. Li, J. Wu, N. Wang, Q. Ding, J. Gao, D. Ling, Molecular design of conjugated small molecule nanoparticles for synergistically enhanced PTT/PDT, Nano-Micro Lett. 12 (1) (2020) 147.
[19] X. Huang, Y. Lu, M. Guo, S. Du, N. Han, Recent strategies for nano-based PTT combined with immunotherapy: from a biomaterial point of view, Theranostics 11 (15) (2021) 7546–7569.
[20] X. Feng, T. Lin, D. Chen, Z. Li, Q. Yang, H. Tian, Y. Xiao, M. Lin, M. Liang, W. Guo, P. Zhao, Z. Guo, Mitochondria-associated ER stress evokes immunogenic cell death through the ROS-PERK-eIF2α pathway under PTT/CDT combined therapy, Acta Biomater. 160 (2023) 211–224.
[21] J. Yang, M. Hou, W. Sun, Q. Wu, J. Xu, L. Xiong, Y. Chai, Y. Liu, M. Yu, H. Wang, Z. P. Xu, X. Liang, C. Zhang, Sequential PDT and PTT using dual-modal single-walled carbon nanohorns synergistically promote systemic immune responses against tumor metastasis and relapse, Adv. Sci. 7 (16) (2020) 2001088.
[22] F.J. Bock, S.W.G. Tait, Mitochondria as multifaceted regulators of cell death, Nat. Rev. Mol. Cell Biol. 21 (2) (2020) 85–100.
[23] J.S. Harrington, S.W. Ryter, M. Plataki, D.R. Price, A.M.K. Choi, Mitochondria in health, disease, and aging, Physiol. Rev. 103 (4) (2023) 2349–2422.
[24] X. Zhu, W. Feng, J. Chang, Y.-W. Tan, J. Li, M. Chen, Y. Sun, F. Li, Temperature-feedback upconversion nanocomposite for accurate photothermal therapy at facile temperature, Nat. Commun. 7 (1) (2016) 10437.
[25] Y. Yang, W. Zhu, Z. Dong, Y. Chao, L. Xu, M. Chen, Z. Liu, 1D coordination polymer nanofibers for low-temperature photothermal therapy, Adv. Mater. 29 (40) (2017) 1703588.
[26] H. Xu, H. Deng, X. Ma, Y. Feng, R. Jia, Y. Wang, Y. Liu, W. Li, S. Meng, H. Chen, NIR-II-absorbing diimmonium polymer agent achieves excellent photothermal therapy with induction of tumor immunogenic cell death, J. Nanobiotechnol. 21 (1) (2023) 132.
[27] V.M. Desai, M. Choudhary, R. Chowdhury, G. Singhvi, Photodynamic therapy induced mitochondrial targeting strategies for cancer treatment: emerging trends and insights, Mol. Pharm. 21 (4) (2024) 1591–1608.

[28] S.-L. Li, P. Jiang, F.-L. Jiang, Y. Liu, Recent advances in nanomaterial-based nanoplatforms for chemodynamic cancer therapy, Adv. Funct. Mater. 31 (22) (2021) 2100243.
[29] P. Zhao, H. Li, W. Bu, A forward vision for chemodynamic therapy: issues and opportunities, Angew Chem Int Ed. 62 (7) (2023) e202210415.
[30] J. Li, Z. You, S. Zhai, J. Zhao, K. Lu, Mitochondria-targeted nanosystem enhances radio–radiodynamic–chemodynamic therapy on triple negative breast cancer, ACS Appl. Mater. Interfaces 15 (18) (2023) 21941–21952.
[31] Y.-N. Hao, W.-X. Zhang, Y.-R. Gao, Y.-N. Wei, Y. Shu, J.-H. Wang, State-of-the-art advances of copper-based nanostructures in the enhancement of chemodynamic therapy, J. Mater. Chem. B 9 (2) (2021) 250–266.
[32] Y. Li, J. Chen, Q. Xia, J. Shang, Y. He, Z. Li, Y. Chen, F. Gao, X. Yu, Z. Yuan, P. Yin, Photothermal Fe_3O_4 nanoparticles induced immunogenic ferroptosis for synergistic colorectal cancer therapy, J. Nanobiotechnol. 22 (1) (2024) 630.
[33] J.-E. Cun, Y. Pan, Z. Zhang, Y. Lu, J. Li, Q. Pan, W. Gao, K. Luo, B. He, Y. Pu, Photo-enhanced upcycling H_2O_2 into hydroxyl radicals by IR780-embedded Fe_3O_4@MIL-100 for intense nanocatalytic tumor therapy, Biomaterials 287 (2022) 121687.
[34] L. Liang, L. Wen, Y. Weng, J. Song, H. Li, Y. Zhang, X. He, W. Zhao, M. Zhan, Y. Li, L. Lu, Y. Xin, C. Lu, Homologous-targeted and tumor microenvironment-activated hydroxyl radical nanogenerator for enhanced chemoimmunotherapy of non-small cell lung cancer, Chem Eng J 425 (2021) 131451.
[35] Q. Chen, C. Li, Q. Wang, Multifunctional nano-biomaterials for cancer therapy via inducing enhanced immunogenic cell death, Small Methods 7 (5) (2023) 2201457.
[36] J. Chen, Y. Zhang, M. Su, Y. Zhu, X. Yang, Nanomedicine-mediated immunogenic cell death and its combination with immune checkpoint blockade therapy, Sci. China Technol. Sci. 67 (8) (2024) 2350–2362.
[37] H. Hu, Z. Dai, F. Zhang, C. Xin, Q. An, X. Meng, Z. Hu, W. Wang, L. Tian, X. Zheng, Metal organic frameworks based intelligent nanoadjuvants for boosting tumor immunotherapy through enhanced ICD and lactic acid regulation, Chem Eng J 479 (2024) 147464.
[38] Q. Xiang, C. Yang, Y. Luo, F. Liu, J. Zheng, W. Liu, H. Ran, Y. Sun, J. Ren, Z. Wang, Near-infrared II nanoadjuvant-mediated chemodynamic, photodynamic, and photothermal therapy combines immunogenic cell death with PD-L1 blockade to enhance antitumor immunity, Small 18 (13) (2022) 2107809.
[39] J. Wang, F. Chen, Y. Jin, R.L. Johnston, Gold–copper aerogels with intriguing surface electronic modulation as highly active and stable electrocatalysts for oxygen reduction and borohydride oxidation, ChemSusChem 11 (8) (2018) 1354–1364.
[40] D.K. Roper, W. Ahn, M. Hoepfner, Microscale heat transfer transduced by surface plasmon resonant gold nanoparticles, J. Phys. Chem. C 111 (9) (2007) 3636–3641.
[41] D.E. Kim, Woolee Chan, Hong Jaemin, Kyung Hyunkwack, Kyu Hwanlee, Hyeon Woobang, Kiyuklee Jaebeumchang, Cheon Sang, Intracellular NO-releasing hyaluronic acid-based nanocarriers: a potential chemosensitizing agent for cancer chemotherapy, ACS Appl. Mater. Interfaces 10 (32) (2018) 26870–26881.
[42] Q. Dan, D. Hu, Y. Ge, S. Zhang, S. Li, D. Gao, W. Luo, T. Ma, X. Liu, H. Zheng, Ultrasmall theranostic nanozymes to modulate tumor hypoxia for augmenting photodynamic therapy and radiotherapy, Biomater. Sci. 8 (3) (2020) 973–987.
[43] M. Reers, S.T. Smiley, C. Mottola-Hartshorn, A. Chen, M. Lin, L.B. Chen, [29] Mitochondrial membrane potential monitored by JC-1 dye, Methods Enzymol. 260 (1995) 406–414.
[44] X. Liu, C.N. Kim, J. Yang, R. Jemmerson, X. Wang, Induction of apoptotic program in cell-free extracts: requirement for dATP and cytochrome c, Cell. 86 (1) (1996) 147–157.
[45] X. Luo, X. Gong, L. Su, H. Lin, Z. Yang, X. Yan, J. Gao, Activatable mitochondria-targeting organoarsenic prodrugs for bioenergetic cancer therapy, Angew Chem Int Ed Engl. 60 (3) (2021) 1403–1410.
[46] D.G. Kirsch, A. Doseff, B.N. Chau, D.-S. Lim, N.C. De Souza-Pinto, R. Hansford, M. B. Kastan, Y.A. Lazebnik, J.M. Hardwick, Caspase-3-dependent cleavage of bcl-2 promotes release of cytochrome c, J. Biol. Chem. 274 (30) (1999) 21155–21161.
[47] E. Swanton, P. Savory, S. Cosulich, P. Clarke, P. Woodman, Bcl-2 regulates a caspase-3/caspase-2 apoptotic cascade in cytosolic extracts, Oncogene 18 (10) (1999) 1781–1787.
[48] S. Qiu, X. Wu, Z. Li, X. Xu, J. Wang, Y. Du, W. Pan, R. Huang, Y. Wu, Z. Yang, Q. Zhou, B. Zhou, X. Gao, Y. Xu, W. Cui, F. Gao, D. Geng, A smart nanoreactor based on an O2-economized dual energy inhibition strategy armed with dual multi-stimuli-responsive “doorkeepers” for enhanced CDT/PTT of rheumatoid arthritis, ACS Nano 16 (10) (2022) 17062–17079.
[49] X. Wang, X. Zhong, Z. Liu, L. Cheng, Recent progress of chemodynamic therapy-induced combination cancer therapy, Nano Today 35 (2020) 100946.
[50] S. Liu, J. Wu, Y. Feng, X. Guo, T. Li, M. Meng, J. Chen, D. Chen, H. Tian, CD47KO/CRT dual-bioengineered cell membrane-coated nanovaccine combined with anti-PD-L1 antibody for boosting tumor immunotherapy, Bioact. Mater. 22 (2023) 211–224.
[51] J. Xue, J.S. Suarez, M. Minaai, S. Li, G. Gaudino, H.I. Pass, M. Carbone, H. Yang, HMGB1 as a therapeutic target in disease, J. Cell. Physiol. 236 (5) (2021) 3406–3419.
[52] Y. Li, R. Xu, Y. Wu, J. Guo, F. Quan, Y. Pei, D. Huang, X. Zhao, H. Gao, J. Liu, Z. Zhang, J. Shi, K. Zhang, Genotype-specific precision tumor therapy using mitochondrial DNA mutation-induced drug release system, Sci. Adv. 9 (39) (2023) eadi1965.
[53] H. Liu, H. Fan, P. He, H. Zhuang, X. Liu, M. Chen, W. Zhong, Y. Zhang, C. Zhen, Y. Li, H. Jiang, T. Meng, Y. Xu, G. Zhao, D. Feng, Prohibitin 1 regulates mtDNA release and downstream inflammatory responses, EMBO J. 41 (24) (2022) e111173.
[54] H. Zhou, W. Zhang, H. Li, F. Xu, E. Yinwang, Y. Xue, T. Chen, S. Wang, Z. Wang, H. Sun, F. Wang, H. Mou, M. Yao, X. Chai, J. Zhang, M.D. Diarra, B. Li, C. Zhang, J. Gao, Z. Ye, Osteocyte mitochondria inhibit tumor development via STING-dependent antitumor immunity, Sci. Adv. 10 (3) (2024) eadi4298.
[55] V. Mysore, X. Cullere, J. Mears, F. Rosetti, K. Okubo, P.X. Liew, F. Zhang, I. Madera-Salcedo, F. Rosenbauer, R.M. Stone, J.C. Aster, U.H. Von Andrian, A. H. Lichtman, S. Raychaudhuri, T.N. Mayadas, FcγR engagement reprograms neutrophils into antigen cross-presenting cells that elicit acquired anti-tumor immunity, Nat. Commun. 12 (1) (2021) 4791.
[56] I. Mantel, B.A. Sadiq, J.M. Blander, Spotlight on TAP and its vital role in antigen presentation and cross-presentation, Mol. Immunol. 142 (2022) 105–119.
[57] F. Morandi, M. Yazdanifar, C. Cocco, A. Bertaina, I. Airoldi, Engineering the bridge between innate and adaptive immunity for cancer immunotherapy: focus on γδ T and NK cells, Cells 9 (8) (2020) 1757.
[58] H. Raskov, A. Orhan, J.P. Christensen, I. Gögenur, Cytotoxic CD8+ T cells in cancer and cancer immunotherapy, Brit J Cancer 124 (2) (2021) 359–367.
[59] Z. Wang, T. You, Q. Su, W. Deng, J. Li, S. Hu, S. Shi, Z. Zou, J. Xiao, X. Duan, Laser-activatable in situ vaccine enhances cancer-immunity cycle, Adv Mater. 35 (52) (2023) 2307193.